

1 **Chromosome counting in the mouse and human zygote using low-invasive super-**  
2 **resolution live-cell imaging**

3

4 \*Yu Hatano<sup>1</sup>, \*Daisuke Mashiko<sup>1</sup>, \*Mikiko Tokoro<sup>1,2</sup>, Tatsuma Yao<sup>1,3</sup>, Ryota Hirao<sup>2</sup>, Hiroya  
5 Kitasaka<sup>2</sup>, Noritaka Fukunaga<sup>2</sup>, Yoshimasa Asada<sup>2</sup>, Kazuo Yamagata<sup>1</sup>

6

7 <sup>1</sup>Faculty of Biology-Oriented Science and Technology, KINDAI University, Kinokawa,  
8 Wakayama, Japan;

9 <sup>2</sup>Asada Institute for Reproductive Medicine, Asada Ladies Clinic, Aichi, Japan;

10 <sup>3</sup>Research and Development Center, Fuso Pharmaceutical Industries, Ltd., Osaka, Japan

11

12 \* These authors contributed to this work equally.

13 **Correspondence should be addressed:** [yamagata@waka.kindai.ac.jp](mailto:yamagata@waka.kindai.ac.jp) (KY)

14

15

16 **Impact Statement**

17 Low-toxic super-resolution observation enables chromosome counting in preimplantation  
18 embryos without cell collection.

19

20 **Abstract**

21 In preimplantation embryos, an abnormal chromosome number causes developmental failure  
22 and a reduction in the pregnancy rate. Conventional chromosome testing methods requiring  
23 biopsy reduce the risk of associated genetic diseases; nevertheless, the reduction in cell number  
24 also reduces the pregnancy rate. Therefore, we attempted to count the chromosomes in mouse  
25 (Slc:ICR) embryos using super-resolution live-cell imaging as a new method of chromosome  
26 counting that does not reduce the cell number or viability. We counted the forty chromosomes  
27 at the first mitosis by injecting embryos with histone H2B-mCherry mRNA under conditions  
28 by which pups could be obtained; however, the results were often an underestimation of  
29 chromosome number and varied by embryo and time point. Therefore, we developed a method  
30 to count the chromosomes via CRISPR/dCas-mediated live-cell fluorescence *in situ*  
31 hybridization targeting the sequence of the centromere region, enabling us to count the  
32 chromosomes more accurately in mouse **and human embryos**. The methodology presented here  
33 may be broadly applied to assisted reproductive technologies, such as those used in livestock  
34 animals/human, as a technique for assessing the chromosomal integrity of embryos prior to  
35 transfer.

## 36 Introduction

37 In preimplantation embryos, the number of chromosomes is correlated with the pregnancy  
38 rate in assisted reproductive technology (ART) and animal breeding (*Magli et al., 2000,*  
39 *Sandalinas et al., 2001, Rubio et al., 2007, Mantikou., 2012, Yao et al., 2018*). In addition,  
40 even if embryos with abnormal chromosome numbers achieve full-term development, they  
41 may exhibit severe genetic disease (e.g., trisomy 21) (*Lejeune et al., 1959*). Therefore,  
42 evaluating chromosome numbers prior to embryo transplantation is important to mitigate these  
43 risks. Conventional chromosomal testing methods such as collecting and disrupting cells,  
44 subsequent spreading of the chromosomes, or scanning the genome using microarrays or next-  
45 generation sequencing can reduce the risk of genetic disease (Hens et al., 2013). Meanwhile,  
46 an associated risk of decreased pregnancy rate consequent to cell harvesting from  
47 chromosomally normal embryos has been reported (*Mastenbroek et al., 2007*). As  
48 approximately 90% of the causes of trisomy 21 are derived from meiosis (*Antonarakis et al.,*  
49 *1991, Freeman et al., 2007*), determining the number of chromosomes immediately following  
50 fertilization may facilitate the application of strategies to reduce the risk of genetic disease by  
51 excluding embryos with abnormal chromosome numbers from transplantation. Nevertheless,  
52 the number of chromosomes in early-stage embryos cannot be evaluated using these techniques  
53 since they are conventionally performed using blastocysts, which contain a sufficient number  
54 of cells to support cell collection. Therefore, the development of a technology that allows real-  
55 time examination of chromosomes immediately following fertilization without reducing the  
56 number of preimplantation embryo cells would represent a breakthrough in ART.

57 Live-cell imaging constitutes a technology for observing the interior of cells in their native  
58 environment. Through low-toxic, long-term live-cell imaging of mouse early embryos using  
59 fluorescence microscopy (*Yamagata 2009a*), we previously demonstrated that the early  
60 division of preimplantation embryos affects subsequent ontogeny. For example, abnormal  
61 chromosome segregation during early division affects development up to the blastocyst stage  
62 (*Mashiko et al., 2020*), resulting in extremely low birth rates following transplantation of 2-  
63 cell stage embryos (*Yamagata et al., 2009b*). However, although obvious abnormalities leading  
64 to the formation of micronuclei could be detected, it was not possible to count the number of  
65 chromosomes owing to limited resolution (*Mashiko et al., 2020*).

66 In recent years, super-resolution microscopes based on various principles have been  
67 proposed and used for imaging cells (i.e., stimulated emission depletion microscopy (STED):  
68 *Hell et al., 1994; Hell et al., 1995*; photoactivated localization microscopy (PALM): *Betzig et*  
69 *al., 2006*; fluorescence photoactivation localization microscopy (FPALM): *Hess et al., 2006*;

70 stochastic optical reconstruction microscopy (STORM): *Rust et al., 2006*; structured  
71 illumination microscopy (SIM): *Gustafsson et al., 2000*; and Airyscan: *Huff, 2015*).  
72 Nevertheless, long-term observation using a super-resolution microscope may be considered  
73 as highly invasive to observed cells. In particular, during the observation of preimplantation  
74 embryos, acquisition of three-dimensional images and repeated irradiation by the laser for time-  
75 lapse imaging causes embryo damage. Thus, fluorescence observation under conditions that  
76 allow the development of embryos to term without prior arrest is important to ensure that the  
77 observed phenomenon is not an artifact caused by dying cells. To this end, we attempted to  
78 identify appropriate long-term live-cell imaging conditions using a disk confocal type  
79 fluorescence microscope to observe early embryogenesis and predict prognosis (*Yamagata et*  
80 *al., 2009a*). In general, confocal microscopy scans a sample at a single plane, thus requiring  
81 substantial time to obtain an image. In addition, application of high-intensity laser energy may  
82 readily discolor the sample or have cytotoxic effects. In comparison, spinning disk confocal  
83 microscopy can overcome these limitations by scanning multiple points through rotation of the  
84 disk and is therefore suitable for live-cell imaging of early embryos. Moreover, super-  
85 resolution has recently been realized using a disk confocal, optical photon reassignment  
86 microscopy (OPRA)-type microscope by optically reducing individual focal points projected  
87 on pinholes using microlenses (super-resolution via optical re-assignment (SoRa): *Azuma and*  
88 *Kei, 2015*).

89 The objective of this study is therefore to develop a technology capable of providing  
90 chromosome counts in preimplantation embryos without requiring cell collection. Using mice,  
91 which have successfully been used as model animals for the study of mammalian embryos and  
92 the establishment of associated techniques, we applied the SoRa system to count chromosomes  
93 of early-stage embryos under conditions that allowed the embryo to maintain full-term  
94 developmental potential following the super-resolution observation. Lastly, we applied this  
95 methodology to human embryo.

96

## 97 **Results**

### 98 **Construction of the SoRa live-cell imaging system and optimization of imaging conditions** 99 **with minimal phototoxicity**

100 We constructed a disk confocal type super-resolution live-cell imaging system to observe  
101 mouse fertilized eggs (**Figure 1**). As the system has a switching mechanism between the  
102 spinning disk with and without microlenses, we can observe the same specimen under these  
103 two different modes. To cover the broad viewing field of the system, a scientific  
104 complementary metal–oxide–semiconductor (sCMOS) image sensor was used and denoise  
105 algorithms (**Boulangier et al., 2009**) were activated at every acquisition to compensate for the  
106 lower sensitivity compared to electron multiplying charge-coupled devices (EMCCD) sensor.  
107 For observation of the first mitosis (approximately 17 h from the pronuclear stage to the end  
108 of the first mitosis), an incubator and gas chamber were set up on the stage for culturing  
109 embryos. A constant room temperature was maintained at 30 °C so that the embryos would not  
110 be affected by outside air.

111 To evaluate the phototoxicity resulting from observation using the constructed SoRa live-  
112 cell imaging system, we focused on the decay of the brightness (fading) of H2B-mCherry  
113 during the observation of early embryos. We injected mRNA encoding histone H2B-mCherry  
114 into fertilized eggs. One plane of the z-axis of the nucleus of the mouse 2-cell stage embryo  
115 was observed for 100 s continuously in streaming mode. Despite observation under the same  
116 conditions, such as excitation laser power, exposure time, and camera sensitivity, a decrease in  
117 signal was observed with SoRa compared to that observed using the conventional disk confocal  
118 microscopy system W1 (time constant 82.4 vs 137 ms, respectively) (**Figure 2A and B**). This  
119 result suggested that the SoRa system requires more stringent conditions to suppress the  
120 phototoxicity than the conventional W1 system, which likely arises because the SoRa system  
121 has a higher light density (power of laser per unit area) than the conventional W1 system.

122 We next searched for conditions that did not affect embryogenesis following observation  
123 with a super-resolution microscope (**Table 1**). We examined the wavelength, laser power, and  
124 time intervals. At an excitation wavelength of 561 nm, laser power of 0.1 mW, and 5 min  
125 intervals, the number of embryos that reached the 2-cell stage was 10/10 (100%) and 8/10  
126 (80%) reached the blastocyst stage. At an excitation wavelength of 561 nm, laser power of 0.1  
127 mW, and 10 min intervals, 5/5 (100%), embryos reached 2 cells and 4/5 (80%) reached the  
128 blastocyst stage. The blastocyst arrival rate under these conditions did not differ from that in  
129 the non-observed group (14/22 (63.6%),  $P = 0.61$ ,  $P = 0.86$ , prop-test). Laser power of 0.2 mW

130 affected the growth up to the blastocyst stage more than 0.1 mW (0.2 mW, 5 min: 0/5 (0%);  
131 0.2 mW, 10 min: 1/5 (20%), prop-test  $P = 0.0086, 0.046$ , respectively). These results suggested  
132 that a laser power of 0.1 mW is suitable for an excitation wavelength of 561 nm. However, at  
133 an excitation wavelength of 488 nm and laser power of 0.1 mW, no embryos reached the  
134 blastocyst stage regardless of the time interval, indicating that an excitation wavelength of 488  
135 nm is more toxic. We therefore utilized the conditions supportive of normal embryo  
136 development following super-resolution observation using a wavelength of 561 nm in  
137 subsequent experiments.

138 To examine whether super-resolution live-cell imaging allowed subsequent full-term  
139 embryo development, 2-cell embryos observed at an excitation wavelength of 561 nm, laser  
140 power of 0.1 mW, and interval of 5 or 10 min were transplanted into the oviduct of  
141 pseudopregnant mice. Notably, pups were obtained under both intervals (5 min (1/7):  $P = 0.53$ ,  
142 10 min (7/15):  $P = 0.78$ , respectively vs. imaging (-) prop-test) (**Table 2; Table 2--figure  
143 supplement 1**). We therefore adopted a 10 min interval as the preferred observation condition.

144 Under the condition that the pups could be obtained (i.e., excitation wavelength 561 nm,  
145 laser power 1 mW, 10 min interval), time-lapse observation was then performed for 17 h until  
146 the completion of the first mitosis (**Figure 3A and B; Figure 3--movie supplement 1**).

147

#### 148 **SoRa system allows observation of the grooves between the sister chromatids**

149 Subsequently, the resolution of the SoRa system was compared with that of the W1 system  
150 using movies captured by each system. Chromosomes could be seen as two separating sister  
151 chromatids by observation using SoRa but not the conventional W1 system. Furthermore, by  
152 performing deconvolution processing on the images acquired with SoRa, the grooves of sister  
153 chromosomes could be separated more clearly (peak-to-peak length:  $618.7 \pm 137.5$  nm)

154 (**Figure 4**). When interphase nuclei were observed, the contrast of the chromatin in the nuclei  
155 could be observed in more detail by imaging using the SoRa system than when using the  
156 conventional W1 system (**Figure 4**).

157

#### 158 **Chromosome segmentation and auto-counting**

159 For counting the number of chromosomes, we attempted the segmentation of M-phase  
160 chromosomes in living cells. Deconvoluted images were acquired using the Tikhonov  
161 regularization algorithm (*Sage et al., 2017*). Images were noise-processed using the Top Hat  
162 filter (*Legland et al., 2016*) and binarized with Otsu's method (*Otsu, 1979*). As a result of

163 automatically counting binarized objects (*Figure 5A; Figure 5—movie supplement 2*), we  
164 were able to count 40 objects (*Figure 5B*). However, a risk existed of recognizing two objects  
165 as one when the chromosomes were close; consequently, the number of chromosomes detected  
166 were varied among the embryos and time points (*Figure 5C*). Although the chromosomes were  
167 clearly separated compared to the results from conventional W1 system observation (*Figure*  
168 *5—figure supplement 2*), the inconsistent counting of individual chromosomes represented a  
169 limitation of this technique.

170

### 171 **Chromosome counting by centromere labeling with live-fluorescence in situ** 172 **hybridization (live-FISH) technology**

173 To overcome the issue of miscounting at sites of overlapping chromosome signals, we sought  
174 to visualize the centromere, a more restricted DNA region in which the distal ends of all  
175 chromosomes are located (*Figure 6A*). Toward this end, CRISPR-mediated live imaging  
176 technology (*Wang et al., 2019*) was performed by targeting the minor satellite sequence, a  
177 repeat sequence constituting the centromere (*Figure 6B*). First, we designed the crRNA based  
178 on the target sequence used in a previous report of ES cells (*Anton et al., 2014*). As counter  
179 staining, major satellite sequence locating pericentromere, a region on a chromosome that is  
180 larger and existing inward than the centromere (*Figure 6A*), was also labeled using TALE  
181 technology (*Miyazari et al., 2013*). As a result, the signals of both minor and major satellites  
182 were observed at the distal ends of metaphase and anaphase chromosomes (*Figure 6C*).  
183 Importantly, when compared to major satellites, the dot-like signals of minor satellites were  
184 more restricted, and overlapping satellites were not detected (*Figure 6C*).

185 Finally, the number of chromosomes at metaphase were counted by combining centromeres  
186 labeled by live-FISH and the SoRa system. Consequently, it was possible to count 40 pairs of  
187 dot-shaped signals (*Figure 7A, B; Figure 7—movie supplement 3 and 4*). Notably, the number  
188 of counted dot-like signals were 40 in all three embryos analyzed, which did not change with  
189 time (*Figure 7C; Figure 7—figure supplement 3*). In contrast, conventional W1 system did  
190 not consistently detect the dot-like signal (*Figure 7—figure supplement 4*).

191

### 192 **Chromosome counting of human embryos**

193 Upon the observation of the initial division of human embryos expressing histone H2B-  
194 mCherry, human chromosomes were more condensed than those of mice, and hence could not  
195 be counted (*Figure 8—figure supplement 5; Figure 8—movie supplement 5*). To apply the  
196 CRISPR-mediated live-fish technology to human embryos, we designed a crRNAs targeting

197 CENPB-Box in the human centromere region (*Iwahara et al., 1998*), injected the  
198 CRISPR/dCas-gRNA complex, and conducted live-fish using the SoRa system. As a result, we  
199 observed 46 pairs of dot-like signals (*Figure 8; Figure 8—movie supplement 6; Figure 8—*  
200 *movie supplement 7*). Subsequently, we examined the two-cell stage human embryo using  
201 next-generation sequencing and confirmed the presence of 46 chromosomes (*Figure 8—figure*  
202 *supplement 6*).

203



## 204 **Discussion**

205 The objective of this study was to establish a method to count the number of chromosomes in  
206 the one-cell zygote without the need for cell collection and fixation. We continuously observed  
207 the first cleavage of fertilized mouse eggs using an OPRA-type disk confocal super-resolution  
208 microscope and identified the observation conditions under which full-term embryos could be  
209 obtained. Depending on the image quality and timing, we succeeded in counting M-phase  
210 chromosomes using these conditions. Moreover, the CRISPR-mediated live-cell imaging of  
211 the minor-satellite region dramatically improved the accuracy of chromosome counting.  
212 Finally, we succeeded in counting the number of chromosomes in living human embryos using  
213 this methodology.

214

## 215 **Implications of phototoxicity assessment and full-term development**

216 When observing a thick sample such as an oocyte, the image becomes darker and the resolution  
217 in the Z-direction becomes lower than that of a thinner sample, such as most somatic cells.  
218 Although these challenges can be overcome by increasing the laser intensity or the number of  
219 images obtained in the Z-axis direction, such measures tend to decrease the embryo viability.  
220 Moreover, the effect of super-resolution imaging on the viability of preimplantation embryos  
221 has not been reported in the few prior studies that utilized such systems (e.g., Airyscan, SIM,  
222 and STED) to observe mouse embryos ([Zielinska et al., 2019](#)). In the present study, because  
223 observations using the SoRa system evinced faster fading of H2B-mCherry, which indicated  
224 higher phototoxicity than that in conventional systems ([Figure 2A and B](#)), we searched for  
225 observation conditions that did not affect the prognosis of the embryo. [Squirrell et al. 1999](#)  
226 reported that embryo phototoxicity could be evaluated by determining the rate of full-term  
227 development following in-utero transplantation of hamster embryos observed using two-  
228 photon excitation microscopy. This method is convincing since it can confirm that the observed  
229 phenomenon is not caused by dying cells. In the same manner, phototoxicity consequent to  
230 observation using a field microscope ([Yamagata et al., 2005](#)) and a disk confocal system  
231 ([Yamagata et al., 2009a](#)) has been evaluated. In these studies, EGFP- $\alpha$ -tubulin and histone  
232 H2B-mRFP1 were injected into fertilized eggs and observed in two colors (excitation  
233 wavelengths: 488 nm/561 nm) using disk confocal microscopy. In comparison, in the present  
234 study, using super-resolution microscopy, we found that cells harvested from 2-cell embryos  
235 could not grow into blastocysts when observed with an excitation wavelength of 488 nm ([Table](#)  
236 [I](#)). Conversely, following observation at an excitation wavelength of 561 nm, the cells

237 successfully developed into blastocysts and full-term embryos (*Table 2*). These findings  
238 suggest that the phenomenon observed at the excitation wavelength of 561 nm did not reflect  
239 the abnormal behavior of cells dying from phototoxicity. Furthermore, as we identified  
240 conditions under which embryo development proceeded to full-term following super-  
241 resolution observation, it should be possible in future experiments to associate phenomena  
242 observed using the SoRa system with the prognosis of embryo development and the acquisition  
243 of offspring.

244

### 245 **Possibilities afforded by super-resolution live-cell imaging of the first mitosis or** 246 **chromatin**

247 In the present study, we observed the first division of the mouse embryo (*Figure 3A and B*).  
248 Failure of chromosomal segregation during the first mitosis constitutes a major factor in the  
249 termination of embryonic development (*Yamagata et al., 2009b, Mashiko et al., 2020*); thus,  
250 detailed observation of the first mitosis using super-resolution live-cell imaging will allow for  
251 the prediction of developmental failure. We have previously identified a mitotic pattern that  
252 causes aneuploidy using a combination of next generation sequencing and low-magnification  
253 live-cell imaging (*Mashiko et al., 2020*). By repeatedly associating super-resolution  
254 observation of the first mitosis with genomic testing by next generation sequencing methods,  
255 it may be possible to clarify the behavior of chromosome segregation, which is prone to  
256 producing chromosome abnormalities.

257 Notably, analysis of the image data obtained in this study revealed that the SoRa system  
258 provided sufficiently high resolution to observe chromatin density at the 2-cell stage (*Figure*  
259 *4*), which suggests that this system offers considerable promise as a research tool. Since we  
260 have established a low-invasive super-resolution observation method, it has become possible  
261 to link the images with chromatin information in combination with conventional methods for  
262 examining chromatin. For example, the combination of a method for detailed observation of  
263 chromatin dynamics that does not affect embryogenesis (*Figure 4*) with the profiles of  
264 chromatin fold structure as observed by chromosome conformation capture (3C)/Hi-C (*Ke et*  
265 *al., 2017*) and transcription as determined by live-imaging (*Bertrand et al., 1998; Park et al.,*  
266 *2014*) will be expected to accelerate chromatin research.

267

### 268 **Application of chromosome counting to zootechnical science and ART**

269 Counting the chromosomes of mouse zygotes from the obtained super-resolution imaging data  
270 (*Figure 5A and B*) successfully allowed the detection of 40 objects (i.e., 40 pairs of sister

271 chromatids) with a risk of miscounting (**Figure 5C**). The concept that chromosome counts  
272 could be obtained using super-resolution microscopy had previously been tested on U2OS cells  
273 (**Gao et al., 2012**); however, the effects on cell viability or risk of miscounting were not  
274 reported. In the present study, by further applying the CRISPR-mediated live-FISH technique  
275 to our super-resolution live-cell imaging system (**Figure 6**), we obtained 40-pairs (mice:  
276 **Figure 7**) and 46-pairs (human: **Figure 8**) of dot signals without measurement error over time.  
277 This suggests that if the chromosomes of livestock/human fertilized eggs could be segmented  
278 in the same manner as mouse embryos and the number of chromosomes can be measured, the  
279 risk of transplanting abnormal ploidy embryos may be reduced. Although chromosome  
280 counting has been attempted by observing the centromere and kinetochore (**Chiang and**  
281 **Lampson, 2013**), to our knowledge, the number of chromosomes has not yet been counted in  
282 living cells. Notably, the human alpha-satellite sequence (**Willard, 1985**) is homologous to the  
283 mouse minor satellite sequence used in the present study, and cattle are also recognized to carry  
284 centromere satDNA (**Macaya et al., 1978; Modi et al., 1993; Modi et al., 1996**). Thus, bovine  
285 embryo chromosomes could also be counted using a gRNA that targets the alpha-satellite.  
286 Taken together, our methodology presented in this report, the combination of SoRa system and  
287 live-FISH technology, can be used in ART and breeding livestock.  
288

## 289 **Material and Methods**

### 290 **Animals**

291 This study conformed to the requirements of the Guide for the Care and Use of Laboratory  
292 Animals. All animal experiments were approved by the Animal Care and Use Committee at  
293 the Research Institute for Kindai University (permit number: KABT-28-001). ICR strain mice  
294 (15-week-old) were obtained from Japan SLC, Inc. (Shizuoka, Japan), and were bred under a  
295 specific pathogen-free environment. Room conditions were standardized with temperature  
296 maintained at 23 °C, relative humidity at 50%, and 12 h/dark: 12 h light cycle. Animals had  
297 free access to water and commercial food pellets. Mice used for the experiments were  
298 euthanized by cervical dislocation.

299

### 300 **Ethics statement**

301 All experiments using human embryos were approved by the Ethics Committee of Asada  
302 Ladies Clinic (Approval number is 2017-05), Kindai-University (Approval number: H27-2-  
303 008), and the Japanese Society of Obstetrics and Gynecology (date of approval /approval  
304 number: 04/25/2018). Informed consent was obtained from all patients who provided embryos  
305 for the study.

### 306 ***In vitro* fertilization**

307 To obtain the unfertilized egg, superovulation was induced in female ICR mice (15 weeks old)  
308 by intraperitoneal injections of 10 IU pregnant mare serum gonadotropin (ASKA Animal  
309 Health Co., Ltd., Tokyo, Japan) and 10 IU human chorionic gonadotropin (hCG) (ASKA  
310 Animal Health) at 48 h intervals. Cumulus-intact oocytes were recovered at euthanasia 15–17  
311 h following hCG injection; these oocytes were arrested at metaphase II of the meiotic cell cycle.  
312 Spermatozoa were collected from the cauda epididymis of male ICR mice (11–16 weeks old)  
313 in 0.2 mL droplets of TYH medium (*Toyoda et al., 1971*) and capacitated by incubation for 1.5  
314 h at 37 °C under 5% CO<sub>2</sub> in humidified air. Cumulus-intact oocytes were collected in 0.2 mL  
315 of TYH medium and inseminated with spermatozoa (final concentration 75 sperm/100 µL).  
316 Upon insemination, oocytes arrested at metaphase II restarted the meiotic cell cycle and  
317 proceeded to interphase in approximately 3 h. After 1.5 h incubation at 37 °C under 5% CO<sub>2</sub>  
318 in humidified air, the cumulus cells were dispersed by brief treatment with hyaluronidase (Type  
319 I-S, 120–300 units/mL; Sigma-Aldrich, St Louis, MO, USA). A total of 30 female and 6 male  
320 mice were used, with three experimental replications (female 10). The obtained fertilized eggs  
321 were frozen. In this process, the eggs of each group used in the experiment were randomized,

322 which was expected to mask individual differences in mice. Frozen eggs were used as follows:  
323 20 for the examination of fading, 57 for the examination of developmental capacity, 45 for the  
324 examination of birth rate, 10 for observation of 1st mitosis, 10 for W1 and SoRa comparison,  
325 10 for chromosome counting using H2B-mCherry, 10 for chromosome counting using  
326 CRISPR-mediated live-FISH, and 20 for measuring the distance between sister chromosomes.  
327

### 328 **Preparation of mRNAs to express proteins of interest**

329 After linearization of the template plasmids (pcDNA3.1-polyA83: *Yamagata et al., 2005*,  
330 pTALYM3 (Addgene #47874): *Miyanari et al., 2013*) at the XhoI (histone H2B-mCherry,  
331 histone H2B-EGFP) and ApaI (pTALYM3) site, mRNA was synthesized using RiboMAX™  
332 Large Scale RNA Production Systems-T7 (Promega, Madison, WI, USA). For efficient  
333 translation of the fusion proteins in embryos, the 5'-end of each mRNA was capped using the  
334 Ribo m7G Cap Analog (Promega), according to the manufacturer's protocol. To circumvent  
335 the integration of template DNA into the embryonic genome, the reaction mixtures for in vitro  
336 transcription were treated with RQ-1 RNase-free DNase I (Promega). Synthesized mRNAs  
337 were treated with phenol-chloroform to remove protein components. The mRNAs were further  
338 purified by filtration using MicroSpin™ S-200 HR columns (Amersham Biosciences,  
339 Piscataway, NJ, USA) to remove unreacted substrates (RNA reaction intermediates) and then  
340 stored at -80 °C until use.

341

### 342 **Preparation of the dCas/gRNA complex**

343 The target sequence of minor satellites of mouse was 5'-ACACTGAAAAACACATTCGT-3'  
344 (*Anton et al., 2014*), while target sequences of alpha satellites of human were 5'-  
345 TTCGTTGGAAAC-3' and 5'-TTCGTTGGAAGC-3'. crRNA and tracrRNA-ATTO550  
346 (Integrated DNA Technologies, Redwood City, CA) hybridized using a T100 thermal cycler  
347 (Bio-Rad Laboratories, Hercules, CA, USA) (94 °C: 5 min, 60 °C: 5 min) were mixed with  
348 dCas protein (Integrated DNA Technologies, Redwood City, CA). The final concentrations of  
349 gRNA and dCas for mice embryos were 20 and 200 ng/μL, respectively, while those of gRNA  
350 and dCas for human embryos were 50 and 500 ng/μL, respectively.

351

### 352 **Microinjection of mRNA or dCas/gRNA complex**

353 Probe injection into fertilized eggs was performed as described previously (*Yamagata et al.,*  
354 *2005*). Briefly, mRNAs were diluted to 10 ng/μL using ultrapure water (Thermo Fisher  
355 Scientific Barnstead Smart2Pure; Waltham, MA, USA) and an aliquot was placed in a

356 micromanipulation chamber. Fertilized eggs (approximately 4–6 h following insemination)  
357 were transferred to HEPES-buffered Chatot-Ziomek-Bavister (CZB) (*Chatot et al., 1989*)  
358 medium in the chamber and injected with mRNA using a piezo-driven manipulator with a  
359 narrow glass pipette (1  $\mu\text{m}$  diameter). Once the mRNA solution had been aspirated into the  
360 pipette, piezo pulses were applied to the fertilized eggs to break the zona pellucida and plasma  
361 membrane. A few picoliters of the solution were introduced into the cytoplasm and the pipette  
362 was removed gently. The mRNA-injected fertilized eggs were incubated at 37 °C under 5%  
363 CO<sub>2</sub> in air for at least 2 h prior to injection to allow time for protein production.

364

### 365 **Imaging**

366 The motor-control (Mac5000; Ludl Electronic Products, Hawthorne, NY, USA) and piezo  
367 control (P-725xDD, PIFOC high dynamics piezo scanner) methods were used to control the Z-  
368 axis direction. However, as the images obtained using the piezo-control method were blurred,  
369 we adopted the motor-control method for subsequent experiments. The fertilized eggs were  
370 transferred to 5  $\mu\text{L}$  droplets of potassium simplex optimization medium with amino acids  
371 (KSOMaa) containing 0.00025% polyvinyl alcohol (P8136-250G; Sigma-Aldrich) and 100  
372  $\mu\text{M}$  ethylenediaminetetraacetic acid on a glass-bottomed dish and placed in an incubation  
373 chamber (Tokai Hit, Shizuoka, Japan) set at 37°C on the microscope stage. A gas mixture of  
374 5% O<sub>2</sub>, 6% CO<sub>2</sub>, and 89% N<sub>2</sub> was introduced into the chamber (138 mL/min). An inverted IX-  
375 73 microscope (Olympus, Tokyo, Japan) was used with an attached Nipkow disk confocal  
376 microscope (CSU-W1 SoRa; Yokogawa Electric, Tokyo, Japan), a Prime95B scientific  
377 complementary metal oxide semiconductor (sCMOS) camera (Teledyne Photometrics, Tuscon,  
378 AZ, USA), and a filter wheel and z-motor (Mac5000; Ludl Electronic Products, Hawthorne,  
379 NY, USA). As our imaging device contained an attached auto x-y stage (Sigma Koki, Tokyo,  
380 Japan), multiple embryos could be monitored simultaneously. The SoRa system can be  
381 switched to the traditional nipkow disk without micro lenses (CSU-W1 mode), allowing  
382 parallel observation of the same sample. A set of imaging systems was placed in a dark room  
383 with the room temperature maintained at 30 °C. Device control was performed using  $\mu$ -  
384 Manager microscopy software (<https://micro-manager.org>). When observing in the Z-  
385 direction, 101 images were taken at 0.5  $\mu\text{m}$  intervals, 25  $\mu\text{m}$  above and below the equatorial  
386 plane of the fertilized egg (total 50  $\mu\text{m}$ ). The observed embryos were subsequently moved to  
387 an incubator to examine their developmental potential.

388

389

## 390 **Image analysis**

391 Line plots were generated using MetaMorph software ver. 7.7.10 (Molecular Devices, San Jose,  
392 CA, USA),  $\mu$ -Manager microscopy software, and the ImageJ/Fiji image analysis platform  
393 (<https://imagej.net/Fiji>). The time constant of the SoRa system was obtained by measuring  
394 the time until H2B-mCherry decayed to 36.8% (derived from the definition of the time constant  
395 in exponential decay and from the reciprocal of the Napier number), and the time constant of  
396 the W1 system was derived from the time until H2B-mCherry decayed to 36.8% after fitting  
397 the exponential curve. Centromere images obtained using the W1 and SoRa systems were  
398 binarized using the yen-method, denoised using median-filter, and the region of interest (ROI)  
399 was detected using Icy (<http://icy.bioimageanalysis.org/>).

400

## 401 **Observation of human embryo**

402 Human embryos used in this study were collected at the Asada-Ladies Clinic that have been  
403 fertilized for therapeutic purposes, are scheduled to be discarded after achieving the goal of  
404 pregnancy and childbirth, and have the consent of the patient for research use as described  
405 above. Frozen fertilized eggs from the clinic were transferred to Kindai University and thawed  
406 using thawing media (VT102, Kitazato BioPharmaCo., Ltd.) prior to the experiment. Thawed  
407 fertilized eggs were placed in a HiGROW OVIT medium (Fuso Pharmaceutical Industries, Ltd.,  
408 Osaka, Japan), and microinjection and super-resolution observations were conducted.

409

## 410 **Chromosome counting/dot signal counting**

411 The FIJI distribution of ImageJ ([Schindelin et al., 2012](#)) was used for image processing.  
412 Deconvolved images were acquired using the Tikhonov regularization algorithm in the  
413 DeconvolutionLab2 plugin ([Sage et al., 2017](#)) with a theoretical point spread function  
414 calculated using the Diffraction PSF 3D plugin. Following deconvolution, these images were  
415 applied to the Top Hat filter in the MorphoLibJ plugin ([Legland et al., 2016](#)) for noise removal  
416 and binarized using Otsu's algorithm. Proximate objects in the image were separated using the  
417 Transform Watershed 3D algorithm in the MorphoLibJ plugin. The dot signals of the minor  
418 satellite were counted using FIJI and FluoRender ([Wan et al., 2012](#);  
419 <https://www.sci.utah.edu/software>).

420

## 421 **Genome sequencing**

422 An Ion ReproSeq PGS kit was used for extraction, amplification, and barcoding of genomic  
423 DNA (A34899, Thermo Fisher Scientific, Waltham, MA, USA). The barcoded samples were

424 evaluated using the Ion Chef System and Ion S5 Next-generation sequencing System (Thermo  
425 Fisher Scientific). The reads were mapped to the human reference genome (hg19) using Bowtie  
426 software (<http://bowtie-bio.sourceforge.net>). We then calculated the moving average of the  
427 mapping read counts within a 10-Mbp window and compared it with normal male/female  
428 genome to identify the number of chromosomes.

429

### 430 **Embryo transfer**

431 Embryo transfer has been described previously (*Yamagata et al., 2009b*). Two-cell mice  
432 embryos were transferred into the oviducts of day 0.5 pseudopregnant mice. At 18 days  
433 following the transfer, cesarean section was performed.

434

### 435 **Sample-size estimation**

436 The blastocyst formation rate in mice is approximately 70–90% and is expected to decrease to  
437 0% to 20% when problems such as environmental or embryo damage occur. We determined  
438 that a total of  $n = 5.08$  embryos were required to test the hypothesis that blastocyst formation  
439 rate is reduced by super-resolution observation by assuming power = 0.8, sig.level = 0.05,  
440 blastocyst ratio of control group = 0.8, blastocyst ratio of observed group = 0.1, one-sided test  
441 and prop-test. In turn, the birth rate of mice is approximately 40–60% and is expected to be  
442 reduced to 0–10% owing to embryonic damage. We calculated that  $n = 11.08$  embryos would  
443 be required to test the hypothesis that super-resolution observation reduced the birth rate by  
444 assuming the power was 0.8, sig.level = 0.05, term development ratio of the control group =  
445 0.5, term ratio of the observed group = 0.05, one-sided test and prop-test. However, the lack of  
446 significant difference under these conditions does not necessarily suggest the lack of effect.  
447 Thus, in the present study, we confirmed whether any abnormalities in blastocyst formation  
448 were present following observation of the embryos under these conditions and considered  
449 whether live offspring could be obtained. Power analysis was performed using R.

450

### 451 **Experimental replication**

452 With super-resolution observation, the number of eggs that could be observed in one  
453 experiment was approximately 10. Thus, the number of eggs used in one experiment was  
454 approximately 5 in each of the two groups (biological replication  $n = 5$ /once). Technical  
455 replication was  $N = 1$  in the examination of fading,  $N = 4$  for blastocyst formation rate,  $N = 5$   
456 for term ratio,  $N = 1$  for first mitosis,  $N = 1$  in the comparison between conventional W1 and  
457 SoRa systems,  $N = 1$  each for chromosome counting by H2B-mCherry mRNA and by CRISPR-



458 mediated live-FISH, and  $N = 2$  for measuring the distance between sister chromosomes. The  
459 technical replication of experiments related to qualitative conclusions and calculation of the  
460 time constant was set to 1. By setting a control group for each experimental replication, we  
461 confirmed that inconsistent observation results were not obtained for each experimental  
462 replication control group.

463

#### 464 **Statistical analysis**

465 One-sided proportion test was performed using the `prop.test` function in R. Wilcoxon Rank sum  
466 test was performed using R.

467 **Competing interests**

468 The authors declare no conflict of interest.

469

470 **Author contributions**

471 Yu Hatano: Methodology, Validation, Formal analysis, Investigation, Resources, Visualization,  
472 manuscript review & editing; Daisuke Mashiko: Data curation, Formal analysis, original  
473 manuscript draft preparation; Mikiko Tokoro: Formal analysis, Investigation, Resources;  
474 Tatsuma Yao: Formal analysis, Software; Ryota Hirao and Hiroya Kitasaka: Investigation,  
475 Resources; Noritaka Fukunaga and Yoshimasa Asada: Conceptualization and Ethical  
476 procedures; Kazuo Yamagata: Conceptualization, Supervision, manuscript review & editing,  
477 Funding acquisition.

478

479 **Acknowledgements**

480 We would like to thank Editage for English language editing. We would like to thank Takuya  
481 Azuma for producing the image of the SoRa W1 switching system. We thank IGENOMIX  
482 JAPAN for genome sequencing.

483

484 **Funding**

485 This work was supported by JSPS KAKENHI Grant Numbers JP25712035, JP25116005,  
486 JP18H05528, and JP18H02357 to KY. The funders had no role in study design, data collection  
487 and interpretation, or the decision to submit the work for publication.

488

## 489 **References**

- 490 **Anton T**, Bultman S, Leonhardt H, Markaki Y. 2014. Visualization of specific DNA sequences  
491 in living mouse embryonic stem cells with a programmable fluorescent CRISPR/Cas  
492 system. *Nucleus* **5**:163–172. DOI: <https://doi.org/10.4161/nucl.28488>
- 493 **Antonarakis SE**. 1991. Parental origin of the extra chromosome in trisomy 21 as indicated by  
494 analysis of DNA polymorphisms. Down Syndrome Collaborative Group. *New England*  
495 *Journal of Medicine* **324**:872–876. DOI: <https://doi.org/10.1056/NEJM199103283241302>
- 496 **Azuma T**, Kei T. 2015. Super-resolution spinning-disk confocal microscopy using optical  
497 photon reassignment. *Optics Express* **23**:15003–15011. DOI:  
498 <https://doi.org/10.1364/OE.23.015003>
- 499 **Bertrand E**, Chartrand P, Schaefer M, Shenoy SM, Singer RH, Long RM. 1998. Localization  
500 of ASH1 mRNA particles in living yeast. *Molecular Cell* **2**:437–445. DOI:  
501 [https://doi.org/10.1016/S1097-2765\(00\)80143-4](https://doi.org/10.1016/S1097-2765(00)80143-4)
- 502 **Betzig E**, Patterson GH, Sougrat R, Lindwasser OW, Olenych S, Bonifacino JS, Davidson MW,  
503 Lippincott-Schwartz J, Hess HF. 2006. Imaging intracellular fluorescent proteins at  
504 nanometer resolution. *Science*, **313**:1642–1645. DOI:  
505 <https://doi.org/10.1126/science.1127344>
- 506 **Boulanger J**, Kervrann C, Bouthemy P, Elbau P, Sibarita J B, Salamero J. 2009. Patch-based  
507 nonlocal functional for denoising fluorescence microscopy image sequences. *IEEE*  
508 *transactions on medical imaging*, 29(2), 442-454. DOI:  
509 <https://doi.org/10.1109/TMI.2009.2033991>
- 510 **Chatot CL**, Ziomek CA, Bavister BD, Lewis JL, Torres I. 1989. An improved culture medium  
511 supports development of random-bred 1-cell mouse embryos in vitro. *Journal of*  
512 *Reproduction and Fertility* **86**:679–688. DOI: <https://doi.org/10.1530/jrf.0.0860679>
- 513 **Chiang T**, Lampson MA. 2013. Counting chromosomes in intact eggs. *Methods in Molecular*  
514 *Biology* **957**:249–253. DOI: [https://doi.org/10.1007/978-1-62703-191-2\\_17](https://doi.org/10.1007/978-1-62703-191-2_17)
- 515 **Fragouli E**, Alfarawati S, Spath K, Babariya D, Tarozzi N, Borini A, Wells D. (2017). Analysis  
516 of implantation and ongoing pregnancy rates following the transfer of mosaic diploid–  
517 aneuploid blastocysts. *Human Genetics*, 136(7), 805-819. DOI:  
518 <https://doi.org/10.1007/s00439-017-1797-4>
- 519 **Freeman SB**, Allen EG, Oxford-Wright CL, Tinker SW, Druschel C, Hobbs CA, O’Leary LA,  
520 Romitti PA, Royle MJ, Torfs CP, Sherman SL. 2007. The National Down Syndrome  
521 Project: design and implementation. *Public Health Reports* 122:62–72. DOI:  
522 <https://doi.org/10.1177/003335490712200109>

- 523 **Gao L**, Shao L, Higgins CD, Poulton JS, Peifer M, Davidson MW, Wu X, Goldstein B, Betzig  
524 E. 2012. Noninvasive imaging beyond the diffraction limit of 3D dynamics in thickly  
525 fluorescent specimens. *Cell* **151**:1370–1385. DOI:  
526 <https://doi.org/10.1016/j.cell.2012.10.008>
- 527 **Gustafsson MG**. 2000. Surpassing the lateral resolution limit by a factor of two using  
528 structured illumination microscopy. *Journal of Microscopy* **198**:82–87. DOI:  
529 <https://doi.org/10.1046/j.1365-2818.2000.00710.x>
- 530 **Hell SW**, Wichmann J. 1994. Breaking the diffraction resolution limit by stimulated emission:  
531 stimulated-emission-depletion fluorescence microscopy. *Optics Letters* **19**:780–782. DOI:  
532 <https://doi.org/10.1364/OL.19.000780>
- 533 **Hell SW**, Kroug M. 1995. Ground-state-depletion fluorescence microscopy: A concept for  
534 breaking the diffraction resolution limit. *Applied Physics B* **60**:495–497. DOI:  
535 <https://doi.org/10.1007/BF01081333>
- 536 **Hens K**, Dondorp W, Handyside A H, Harper J, Newson A J, Pennings G, ... & de Wert G.  
537 2013. Dynamics and ethics of comprehensive preimplantation genetic testing: a review of  
538 the challenges. *Human Reproduction Update*, 19(4), 366-375. DOI:  
539 <https://doi.org/10.1093/humupd/dmt009>
- 540 **Hess ST**, Girirajan TP, Mason MD. 2006. Ultra-high resolution imaging by fluorescence  
541 photoactivation localization microscopy. *Biophysical Journal* **91**:4258–4272. DOI:  
542 <https://doi.org/10.1529/biophysj.106.091116>
- 543 **Huff J**. 2015. The Airyscan detector from ZEISS: confocal imaging with improved signal-to-  
544 noise ratio and super-resolution. *Nature Methods* **12**: i–ii. DOI:  
545 <https://doi.org/10.1038/nmeth.f.388>
- 546 **Iwahara J.**, Kigawa T., Kitagawa K., Masumoto H., Okazaki T., & Yokoyama S. (1998). A  
547 helix–turn–helix structure unit in human centromere protein B (CENP - B). *The EMBO*  
548 *journal*, 17(3), 827-837.
- 549 **Ke Y**, Xu Y, Chen X, Feng S, Liu Z, Sun Y, Yao X, Li F, Zhu W, Gao L, Chen H, Du Z, Xie  
550 W, Xu X, Huang X, Jiang L.. 2017. 3D chromatin structures of mature gametes and  
551 structural reprogramming during mammalian embryogenesis. *Cell* **170**:367–381. DOI:  
552 <https://doi.org/10.1016/j.cell.2017.06.029>
- 553 **Legland D**, Arganda-Carreras I, Andrey P. 2016. MorphoLibJ: integrated library and plugins  
554 for mathematical morphology with ImageJ. *Bioinformatics* **32**:3532–3534. DOI:  
555 <https://doi.org/10.1093/bioinformatics/btw413>

- 556 **Lejeune J**, Gauthier M, Turpin R. 1959. [Human chromosomes in tissue culture]. *Comptes*  
557 *Rendus Hebdomadaires des Séances de l'Académie des Sciences* **248**:602–603.
- 558 **Macaya G**, Cortadas J, Bernardi G. 1978. An analysis of the bovine genome by density-  
559 gradient centrifugation. Preparation of the dG+dC-rich DNA components. *European*  
560 *Journal of Biochemistry* **84**:179–188 DOI: [https://doi.org/10.1111/j.1432-](https://doi.org/10.1111/j.1432-1033.1977.tb11565.x)  
561 [1033.1977.tb11565.x](https://doi.org/10.1111/j.1432-1033.1977.tb11565.x)
- 562 **Magli MC**, Jones GM, Gras L, Gianaroli L, Dorman I, Trounson AO. 2000. Chromosome  
563 mosaicism in day 3 aneuploid embryos that develop to morphologically normal blastocysts  
564 in vitro. *Human Reproduction* **15**:1781–1786. DOI:  
565 <https://doi.org/10.1093/humrep/15.8.1781>
- 566 **Mantikou E**, Wong KM, Repping S, Mastenbroek S. 2012. Molecular origin of mitotic  
567 aneuploidies in preimplantation embryos. *Biochimica Biophysica Acta* **1822**:1921–1930.  
568 DOI: <https://doi.org/10.1016/j.bbadis.2012.06.013>
- 569 **Mashiko D**, Ikeda Z, Yao T, Tokoro M, Fukunaga N, Asada Y, Yamagata K. 2020.  
570 Chromosome segregation error during early cleavage in mouse pre-implantation embryo  
571 does not necessarily cause developmental failure after blastocyst stage. *Scientific Reports*  
572 **10**:854. DOI: <https://doi.org/10.1038/s41598-020-57817-x>
- 573 **Mastenbroek S**, Twisk M, van Echten-Arends J, Sikkema-Raddatz B, Korevaar JC, Verhoeve  
574 HR, Vogel NEA, Arts EGJM, de Vries JWA, Bossuyt PM, Buys CHCM, Henieman MJ,  
575 Repping S, van der Veen F. 2007. In vitro fertilization with preimplantation genetic  
576 screening. *New England Journal of Medicine* **357**:9–17. DOI:  
577 <https://doi.org/10.1056/NEJMoa067744>
- 578 **Miyanari Y**, Ziegler-Birling C, Torres-Padilla ME. 2013. Live visualization of chromatin  
579 dynamics with fluorescent TALEs. *Nature Structural & Molecular Biology* **20**:1321–1324.  
580 DOI: <https://doi.org/10.1038/nsmb.2680>.
- 581 **Modi WS**, Gallagher DS, Womack JE. 1993. Molecular organization and chromosomal  
582 localization of six highly repeated DNA families in the bovine genome. *Animal*  
583 *Biotechnology* **4**:143–161. DOI: <https://doi.org/10.1080/10495399309525793>
- 584 **Modi WS**, Gallagher DS, Womack JE. 1996. Evolutionary histories of highly repeated DNA  
585 families among the Artiodactyla (Mammalia). *Journal of Molecular Evolution* **42**:337–349.  
586 DOI: <https://doi.org/10.1007/BF02337544>
- 587 **Otsu N**, 1979. A Threshold Selection Method from Gray-Level Histograms. in *IEEE*  
588 *Transactions on Systems, Man, and Cybernetics*. 9(1):62-66. DOI: [https://doi.org/](https://doi.org/10.1109/TSMC.1979.4310076)  
589 [10.1109/TSMC.1979.4310076](https://doi.org/10.1109/TSMC.1979.4310076).

- 590 **Park, HY**, Lim H, Yoon YJ, Follenzi A, Nwokafor C, Lopez-Jones M, Meng X, Singer RH.  
591 2014. Visualization of dynamics of single endogenous mRNA labeled in live mouse.  
592 *Science* **343**:422–424. DOI: <https://doi.org/10.1126/science.1239200>
- 593 **Rubio C**, Rodrigo L, Mercader A, Mateu E, Buendía P, Pehlivan T, vioria T, De los Santos,  
594 MJ, Simón C, Remohí J, Pellicer A. 2007. Impact of chromosomal abnormalities on  
595 preimplantation embryo development. *Prenatal Diagnosis* **27**:748–756. DOI:  
596 <https://doi.org/10.1002/pd.1773>
- 597 **Rust MJ**, Bates M, Zhuang X. 2006. Sub-diffraction-limit imaging by stochastic optical  
598 reconstruction microscopy (STORM). *Nature Methods* **3**:793–795. DOI:  
599 <https://doi.org/10.1038/nmeth929>
- 600 **Sage D**, Donati L, Soulez F, Fortun D, Schmit G, Seitz A, Guiet R, Vonesch C, Unser M. 2017.  
601 DeconvolutionLab2: An open-source software for deconvolution microscopy. *Methods*  
602 **115**:28–41. DOI: <https://doi.org/10.1016/j.ymeth.2016.12.015>
- 603 **Sandalinas M**, Sadowy S, Akikani M, Calderon G, Cohen , Munné S. 2001. Developmental  
604 ability of chromosomally abnormal human embryos to develop to the blastocyst stage.  
605 *Human Reproduction* **16**:1954–1958. DOI: <https://doi.org/10.1093/humrep/16.9.1954>
- 606 **Schindelin J**, Arganda-Carreras I, Frise E, Kaynig V, Longair M, Pietsch T, Preibisch S,  
607 Rueden C, Saalfeld S, Schmid B, Tinevez JY, White DJ, Hartenstein V, Eliceiri K,  
608 Tomancak P, Cardona A. 2012. Fiji: an open-source platform for biological-image analysis.  
609 *Nature Methods* **9**:676–82. DOI: <https://doi.org/10.1038/nmeth.2019>
- 610 **Squirrell JM**, Wokosin DL, White JG, Bavister BD. 1999. Long-term two-photon  
611 fluorescence imaging of mammalian embryos without compromising viability. *Nature*  
612 *Biotechnology* **17**:763–767. DOI: <https://doi.org/10.1038/11698>
- 613 **Toyoda Y**, Yokoyama M, Hoshi T. 1971. Studies on the fertilization of mouse eggs *in*  
614 *vitro*. *Japanese Journal of Animal Reproduction* **16**, 147–151. DOI:  
615 <https://doi.org/10.1262/jrd1955.16.147>
- 616 **Wan Y**, Otsuna H, Chien CB, Hansen C. 2012. FluoRender: an application of 2D image space  
617 methods for 3D and 4D confocal microscopy data visualization in neurobiology research.  
618 In *2012 IEEE Pacific Visualization Symposium* (pp. 201–208). IEEE, New York. DOI:  
619 <https://doi.org/10.1109/PacificVis.2012.6183592>
- 620 **Wang H**, Nakamura M, Abbott TR, Zhao D, Luo K, Yu C, Nguyen CM, Lo A, Daley TP, La  
621 Russa M, Liu Y, Qi LS. 2019. CRISPR-mediated live imaging of genome editing and  
622 transcription. *Science* **365**.6459:1301–1305. DOI: <https://doi.org/10.1126/science.aax7852>
- 623 **Willard HF**. 1985. Chromosome-specific organization of human alpha satellite DNA.

- 624 *American Journal of Human Genetics* **37**:524–532 DOI: <https://doi.org/10.1016/0888->  
625 [7543\(87\)90103-0](https://doi.org/10.1016/0888-7543(87)90103-0)
- 626 **Yamagata K**, Suetsugu R, Wakayama T. 2009a. Long-term, six-dimensional live-cell imaging  
627 for the mouse preimplantation embryo that does not affect full-term development. *Journal*  
628 *of Reproduction and Development* **55**:343–350. DOI: <https://doi.org/10.1262/jrd.20166>
- 629 **Yamagata K**, Suetsugu R, & Wakayama T. 2009b. Assessment of chromosomal integrity using  
630 a novel live-cell imaging technique in mouse embryos produced by intracytoplasmic sperm  
631 injection. *Human reproduction*, 24(10), 2490-2499. DOI:  
632 <https://doi.org/10.1093/humrep/dep236>
- 633 **Yamagata K**, Yamazaki T, Yamashita M, Hara Y, Ogonuki N, Ogura A. 2005. Noninvasive  
634 visualization of molecular events in the mammalian zygote. *Genesis* **43**:71–79. DOI:  
635 <https://doi.org/10.1002/gene.20158>
- 636 **Yao T**, Suzuki R, Furuta N, Suzuki Y, Kabe K, Tokoro M, Sugawara A, Yajima A, Nagasawa  
637 T, Matoba S, Yamagata K, Sugimura S. 2018. Live-cell imaging of nuclear–chromosomal  
638 dynamics in bovine in vitro fertilised embryos. *Scientific Reports* **8**:7460. DOI:  
639 <https://doi.org/10.1038/s41598-018-25698-w>
- 640 **Zielinska AP**, Bellou E, Sharma N, Frombach AS, Seres KB, Gruhn JR, Blayner M, Eckel H,  
641 Moltrecht r, Elder K, Hoffman ER, Schuh M. 2019. Meiotic kinetochores fragment into  
642 multiple lobes upon cohesin loss in aging eggs. *Current Biology* **29**:3749–3765.e7. DOI:  
643 <https://doi.org/10.1016/j.cub.2019.09.006>

644

645 **Figure legends**

646 **Figure 1.** SoRa live-cell imaging system. Photograph (left) and list (right) of the equipment for  
647 imaging. A conventional inverted microscope was attached to a Nipkow disk confocal unit,  
648 sCMOS camera, Z-motor, and XY auto stage. All devices were controlled using a micro-  
649 manager. Embryos were cultured in a CO<sub>2</sub> incubator at this stage. The Nipkow disk confocal  
650 unit can switch between a conventional unit without micro lenses and a unit with micro lenses  
651 (lower left).

652

653 **Figure 2.** Assessment of the phototoxicity of super-resolution imaging. **(A)** Photographs of 2-  
654 cell nuclei obtained using the W1 (upper panels) and SoRa (below panels) systems. bar: 1  $\mu$ m.  
655 **(B)** Graph of the brightness change.

656

657 **Figure 3.** Super-resolution live-cell imaging of the first mitosis using chromosome counting  
658 by H2B-mCherry mRNA was the SoRa system. **(A)** Schematic diagram of super-resolution  
659 imaging of the first mitosis. **(B)** Super-resolution imaging of the first mitosis in mouse embryos.  
660 The upper panels show the bright-field images. Middle panels show the histone H2B-mCherry  
661 images of the x-y plane, and the panels below show that of the x-z plane. See also  
662 Supplementary movie 1.

663

664 **Figure 4.** The SoRa system enables higher resolution imaging than the conventional W1  
665 system. **(A)** Left six panels show images of the metaphase of an embryo. From left to right, the  
666 image was obtained using W1 (x-y and x-z), SoRa (x-y and x-z), and SoRa (x-y and x-z;  
667 deconvoluted). The right three panels show enlargements of the rectangular area (red). The  
668 right three graphs show the relative intensity on the yellow dashed line. **(B)** The left six panels  
669 show images of the interphase of a 2-cell embryo. The right three panels show enlargements  
670 of the rectangular area (red).

671

672 **Figure 5.** Chromosome counting using H2B-mCherry mRNA. **(A)** The left panel shows the  
673 H2B-mCherry signal. The right image shows the processed image. **(B)** Each panel shows the  
674 recognized object. The white arrowheads indicate a processed chromosome with a risk of  
675 miscount. **(C)** Relationship between the number of recognized objects and time from nuclear  
676 envelope breakdown (NEBD). See also Supplementary Movie 2 and Supplementary Figure 2.

677

678 **Figure 6.** Chromosome counting by CRISPR-mediated live-FISH. **(A)** The left panel shows



679 the illustrated chromosome; the black area shows the mouse centromere region. The right panel  
680 shows the repeated sequence; the underlined sequence shows the sequence targeted by gRNA.  
681 (B) Illustrated scheme of CRISPR-mediated live-cell imaging. The ATTO550 probe was added  
682 to tracrRNA. (C) Snapshot of Histone H2B-mCherry, TALMaj-mClover3, and minor satellite  
683 targeted gRNA using the SoRa system.

684

685 **Figure 7.** CRISPR-mediated live-cell imaging of the centromere region in the mouse  
686 preimplantation embryo. (A) Left panel shows the centromere region and right panel shows the  
687 segmented image. (B) Segmented 40 centromere pairs. (C) The number of pairs of dot signals  
688 was measured at three points prior to the start of anaphase ( $t = 0$ ). See also Supplementary  
689 Figures 3 and 4.

690

691 **Figure 8.** CRISPR-mediated live-cell imaging of the centromere region of the human  
692 preimplantation embryo. (A) The left panel shows the centromere region while the right shows  
693 the segmented image. (B) Segmented 46 centromere pairs. (C) The number of pairs of dot  
694 signals was measured at three points prior to the start of anaphase ( $t = 0$ ).

695

## 696 **Table captions**

697 **Table 1.** Developmental capacity of the preimplantation embryo following super-resolution  
698 imaging.

699 From left to right column: injected mRNA, excitation wavelength of the laser (nm), optical  
700 intensity (mW), time interval (min), imaging period (h), number of embryos examined, number  
701 of 2-cell embryos, and number of blastocysts.

702

703 **Table 2.** Full-term development of transferred embryos following super-resolution imaging.

704 From left to right column: injected mRNA, excitation wavelength of the laser (nm), optical  
705 intensity (mW), time interval (min), imaging period (h), number of embryos examined, number  
706 of 2-cell stage embryos, number of recipients (transferred mice), number of transferred  
707 embryos, and number of pups. See also Supplementary figure 1.

708

709

710

711

712

713 **Additional files**

714

715 **Supplementary Movie 1 (Related to Figure 3).** Super-resolution observation of the first  
716 mitosis of a mouse embryo. The left panel shows the movie from bright field (BF) imaging  
717 while the right shows the movie of the histone H2B-mCherry signal.

718

719 **Supplementary Movie 2 (Related to Figure 5).** Three-dimensional (3D) construction of  
720 segmented chromosomes. Rotated 3D images of the histone H2B-mCherry signal (left) and  
721 processed image (right) are shown.

722

723 **Supplementary Movie 3 (Related to Figure 7).** Live-cell imaging using minor satellite  
724 targeted gRNA. Imaging of the minor satellite region for approximately 17 h from the one-cell  
725 to two-cell stage.

726

727 **Supplementary Movie 4 (Related to Figure 7).** Three-dimensional (3D) construction of the  
728 segmented centromere region. Rotated 3D images of CRISPR-mediated minor satellite signal  
729 (left) and the segmented centromere region (right).

730

731 **Supplementary Movie 5 (Related to Figure 8).** Live-cell imaging of human embryo using  
732 histone H2B-mCherry. The left panel shows the bright-field movie while the right shows the  
733 movie of histone H2B-mCherry.

734

735 **Supplementary Movie 6 (Related to Figure 8).** Live-cell imaging of human embryo using  
736 CRISPR/dCas imaging system. Using alpha-satellite targeting gRNA, the movie of the  
737 centromere was obtained.

738

739 **Supplementary Movie 7 (Related to Figure 8).** Three-dimensional (3D) construction of the  
740 segmented centromere region of human embryo. Rotated 3D images of CRISPR-mediated  
741 alpha satellite signal (left) and the segmented centromere region (right).

742

743 **Supplementary Figure 1 (Related to Table 2).** Two-cell stage embryo prior to transplantation  
744 and pups obtained following transplantation. (A) Representative image of the 2-cell embryo  
745 following observation with an excitation laser at 561 nm, laser power 0.1 mW, and interval 10  
746 min/imaging (-). (B) Representative image of the pups obtained following super-resolution

747 imaging. The upper panel shows images of pups derived from imaging (–) and the lower shows  
748 an image of pups derived from imaging (+).

749

750 **Supplementary Figure 2 (Related to Figure 5).** Chromosome counting using the  
751 conventional W1 system. (A) The left panel shows the H2B-mCherry signal. The right image  
752 shows the segmented image. (B) Each panel shows the recognized object. (C) Relationship  
753 between the number of recognized objects and time from nuclear envelope breakdown (NEBD).

754

755 **Supplementary Figure 3 (Related to Figure 7).** Minor satellite signal of CRISPR-mediated  
756 live-cell imaging. Imaging of a minor satellite with the start of anaphase at  $t = 0$ . An image of  
757 the three time points from each of three embryos is shown.

758

759 **Supplementary Figure 4 (Related to Figure 7).** Comparison of detected signal of centromere  
760 between SoRa system and W1 system. Upper panels show the binarized images of CRISPR-  
761 mediated centromere images obtained using the SoRa system (white) and detected signals  
762 (green). Bottom panels show the binarized images of CRISPR-mediated centromere images  
763 obtained using the W1 system (white) and detected signals (green). The number in the lower  
764 left is the number of dot signals detected.

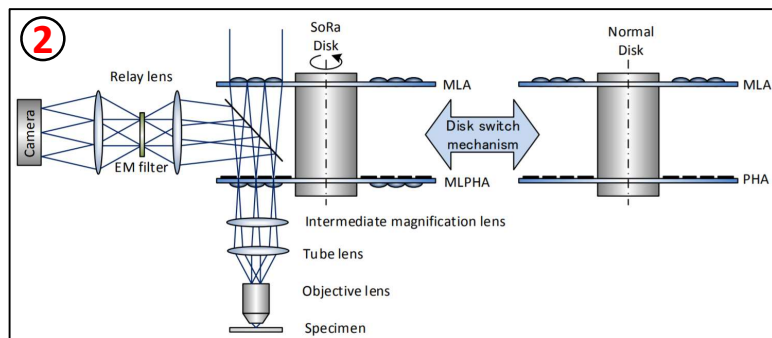
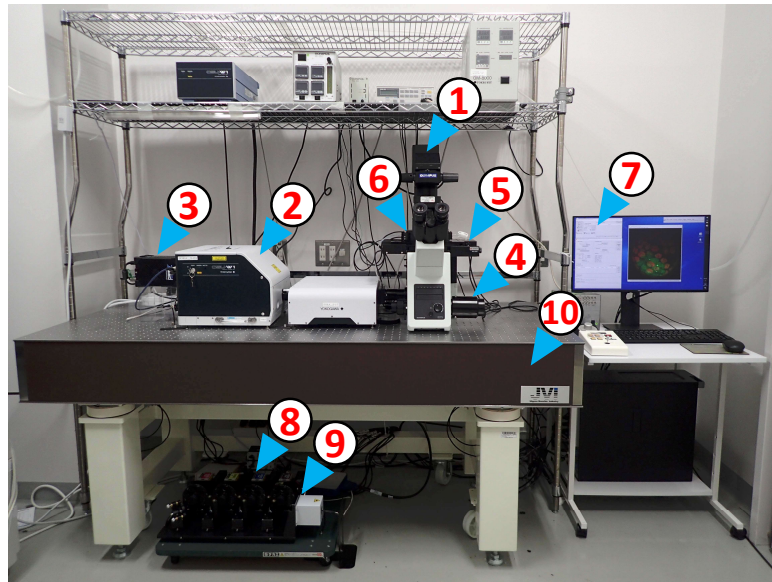
765 **Supplementary Figure 5 (Related to Figure 8)** Super-resolution imaging of human embryo  
766 using H2B-mCherry. Upper panels show the bright-field images, middle panels show the x-y  
767 images of H2B-mCherry, bottom panels show the x-z images of H2B-mCherry, respectively.

768

769 **Supplementary Figure 6 (Related to Figure 8)** Genome sequencing of human embryo. The  
770 result of genome sequencing of observed embryo (blue) was compared to control embryo (red:  
771 female) with no chromosomal abnormalities. The vertical axis represents normalized read, and  
772 the horizontal axis represents chromosome number.

773

774



No.	Devices	Manufacturer	Model
1	Inverted microscope	Olympus	IX-73
2	Nipkow disk Confocal unit	Yokogawa electric	CSU-W1 SoRa
3	sCMOS camera	Photometrics	Prime 95B
4	Z motor	Ludl	Mac5000
5	XY auto stage	Sigmakoki	BIOS-206T
6	CO <sub>2</sub> incubator	Tokai hit	MI-IBC
7	Software	<a href="https://micro-manager.org">https://micro-manager.org</a>	Micro-Manager
8	Lasers	Coherent	405 nm 488 nm 561 nm 640 nm
9	Laser combiner	Sigmakoki	-
10	Vibration isolation table	Nippon boushin industry	SK-AS-1875T

Figure 1.

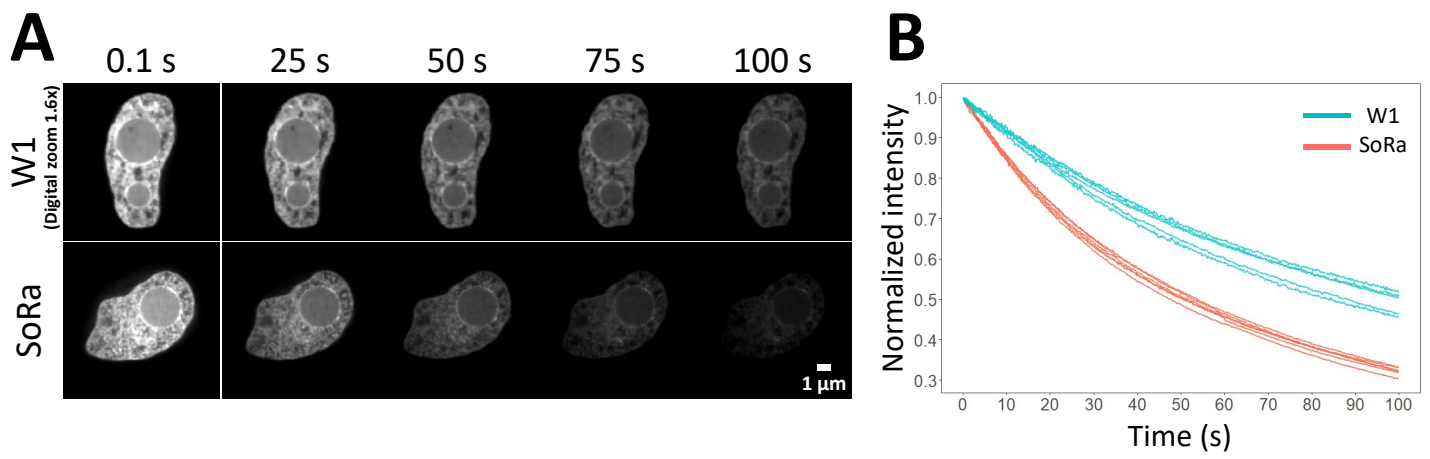


Figure 2.

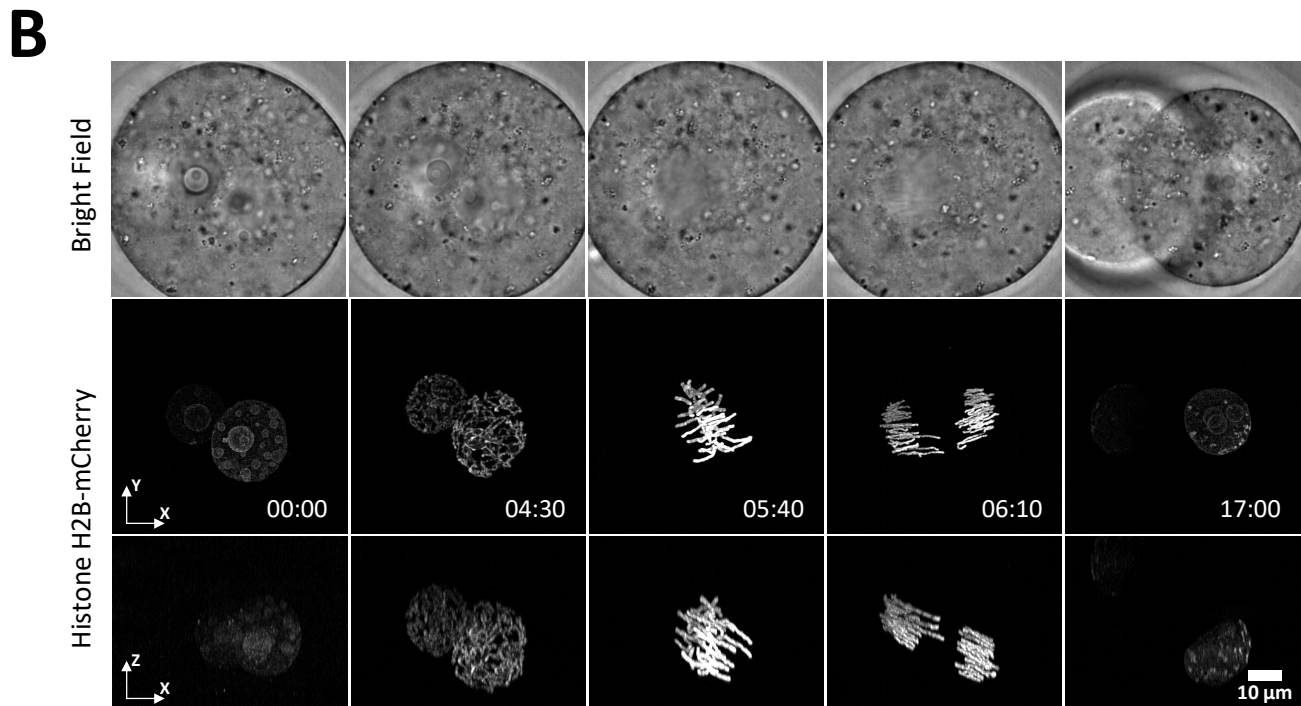
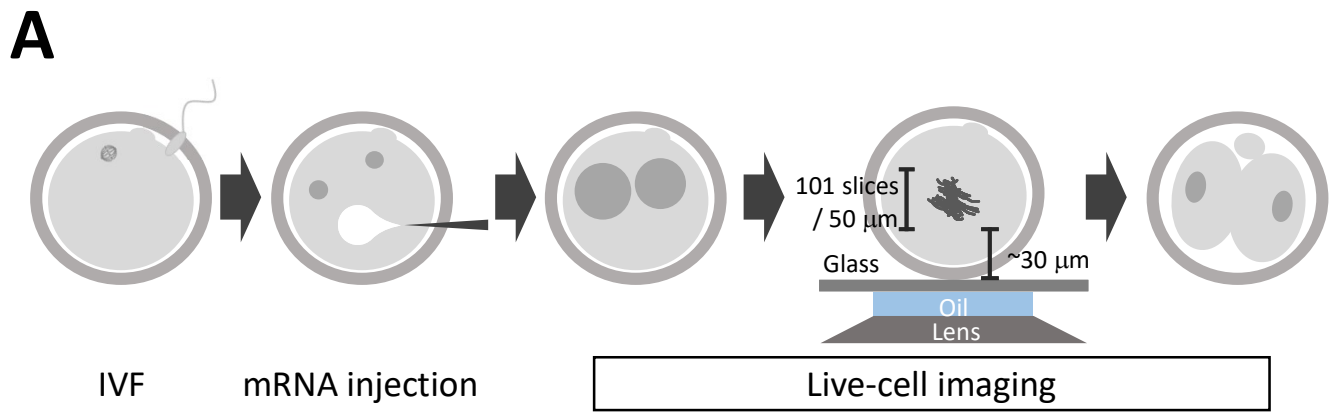


Figure 3.

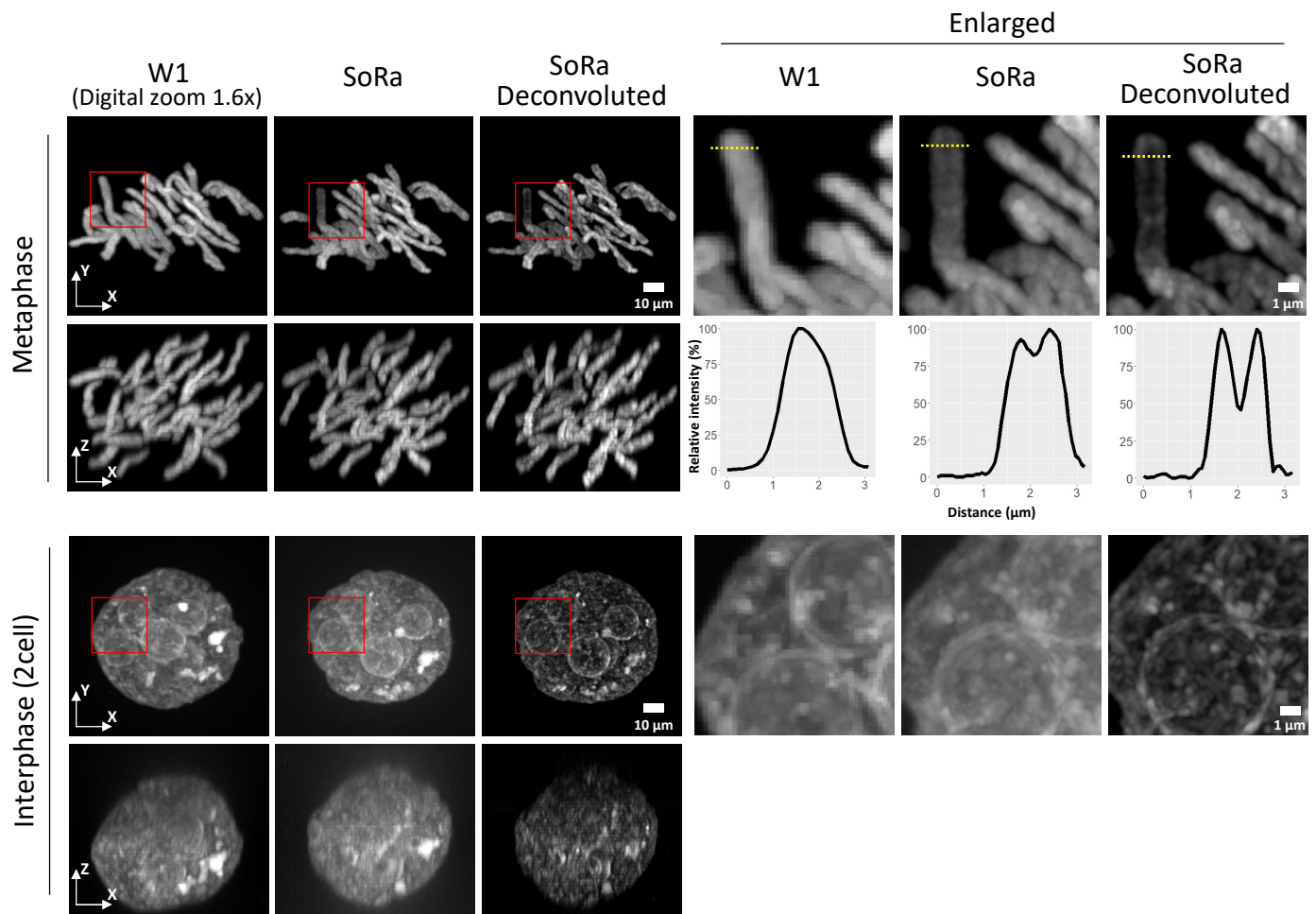
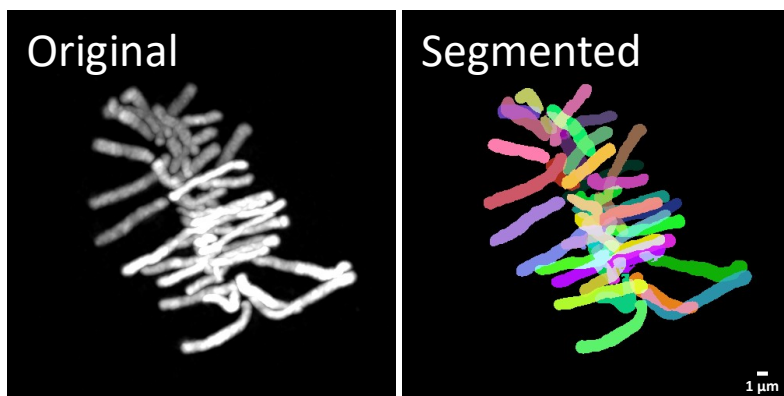
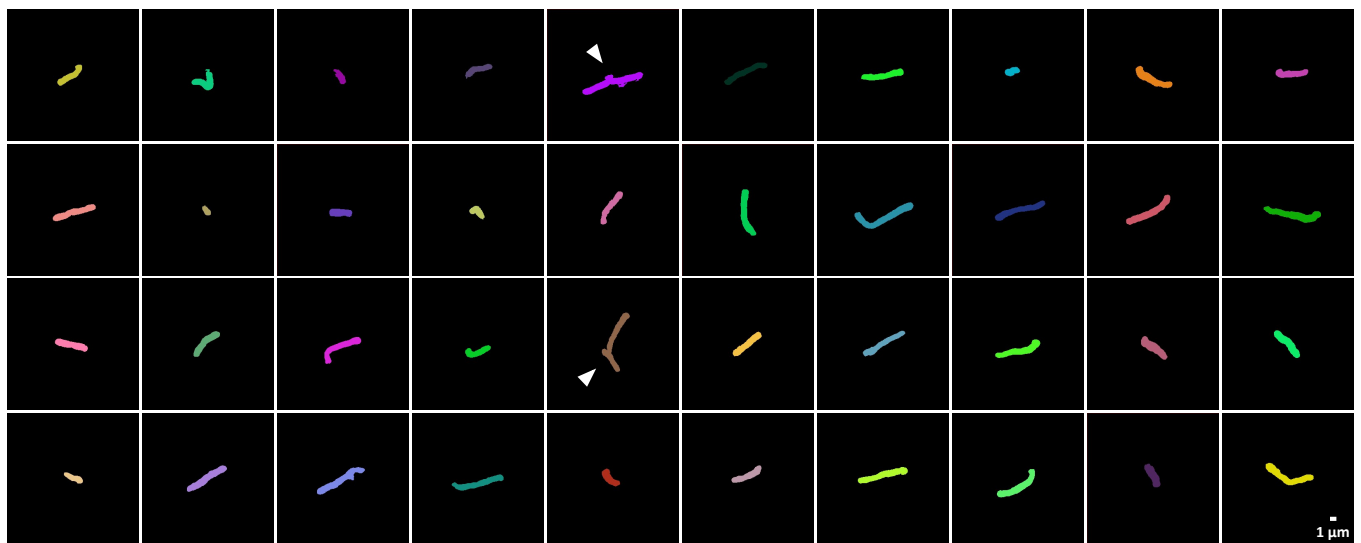


Figure 4.

**A**



**B**



**C**

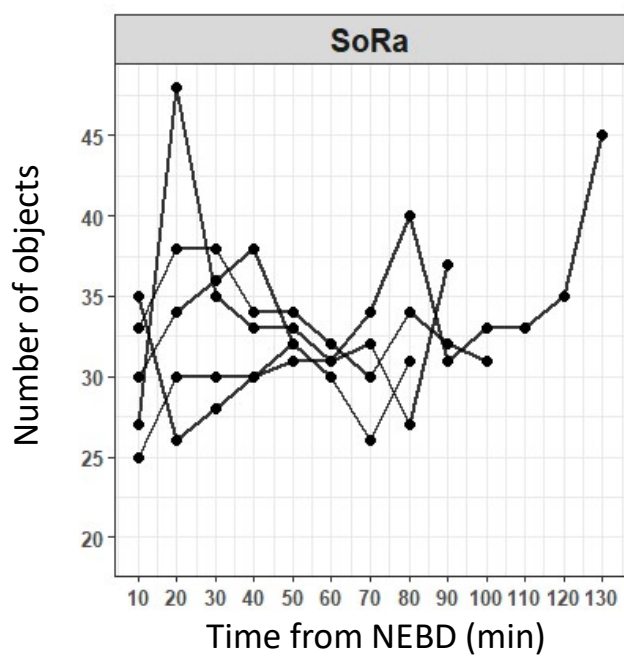


Figure 5.



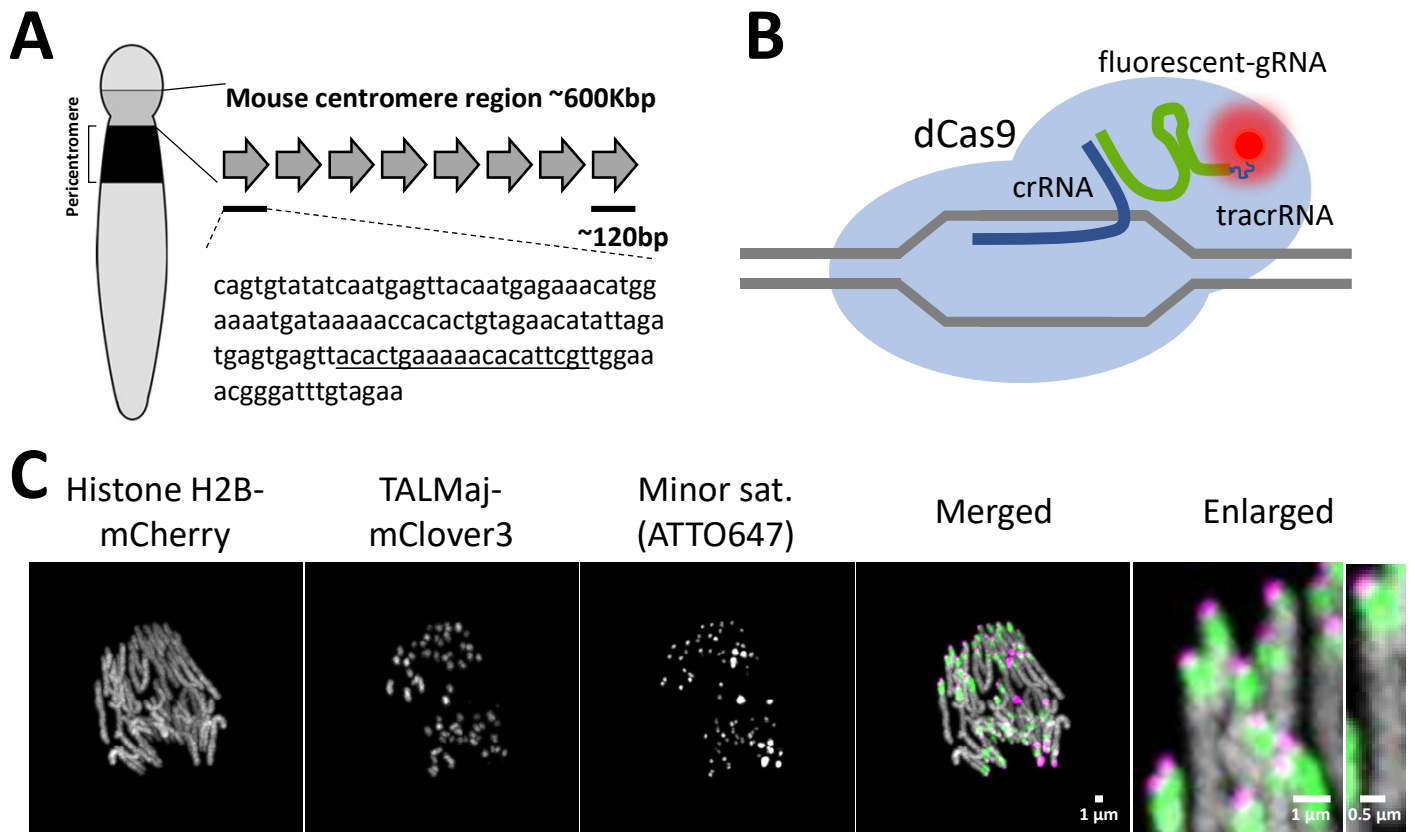


Figure 6.

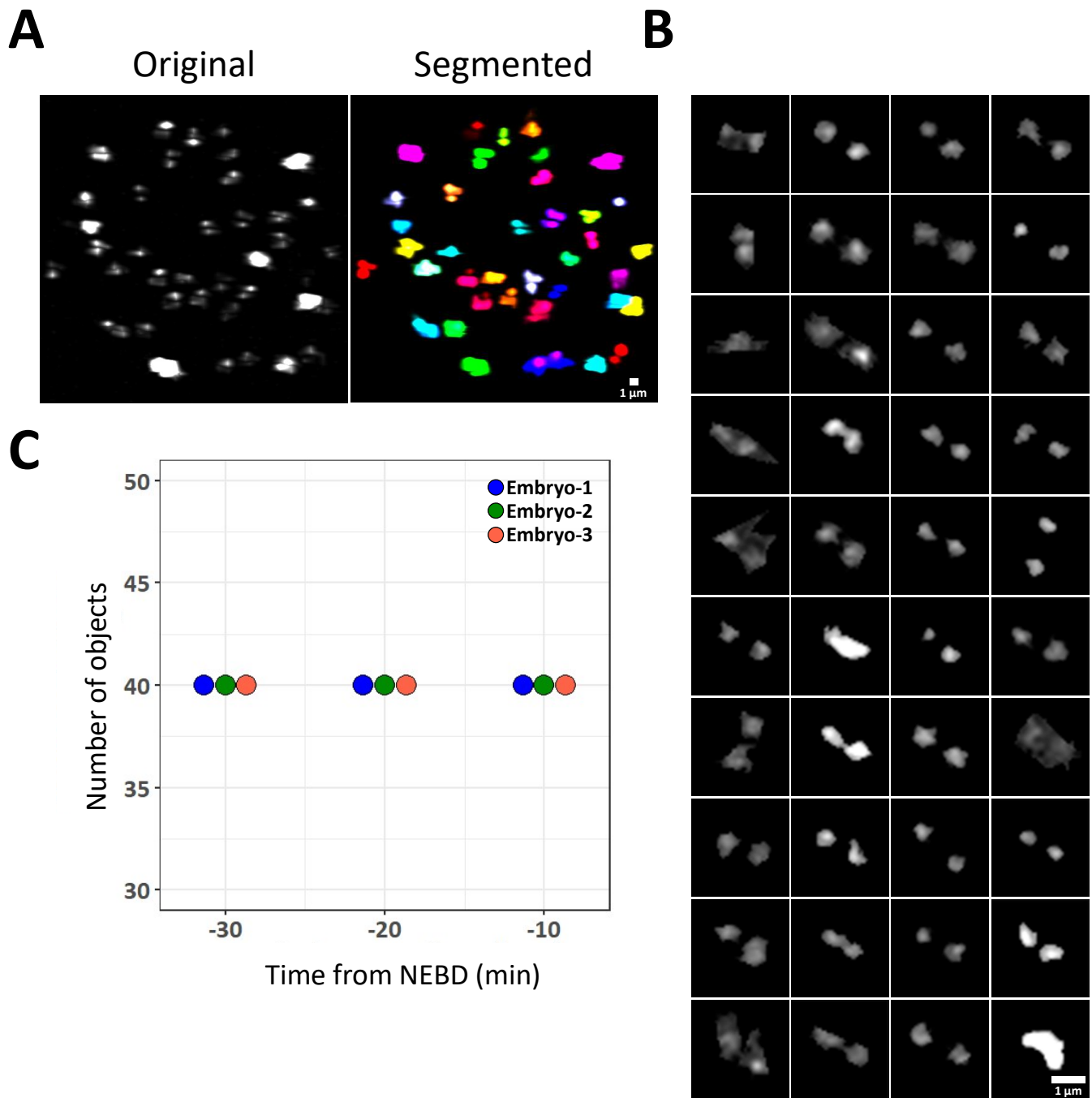


Figure 7.

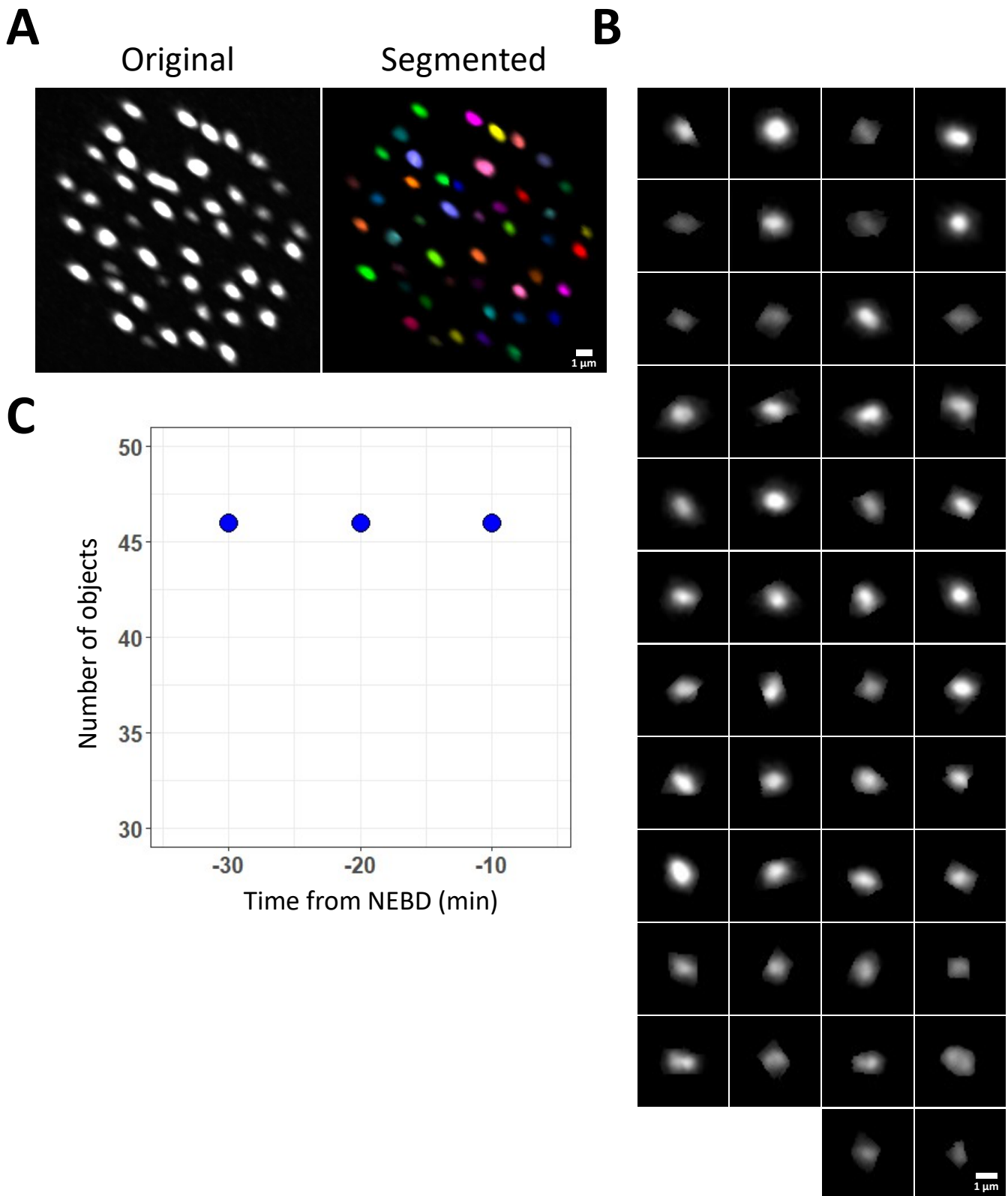


Figure 8.

Table 1. Developmental capacity of the preimplantation embryo following super-resolution imaging

mRNA injected	Optical wavelength (nm)	Optical intensity (mW)	Time intervals (min)	Imaging period (h)	No. of embryos examined	No. (%) of 2-cell embryos	No. (%) of blastocysts
Histone H2B-mCherry	-	-	-	-	22	21 (95.4)	14 (63.6)
	561	0.1	5	17	10	10 (100)	8 (80)
	561	0.1	10	17	5	5 (100)	4 (80)
	561	0.2	5	17	5	0 (0)	0 (0)
	561	0.2	10	17	5	4 (80)	1 (20)
Histone H2B-EGFP	-	-	-	-	7	7 (100)	7 (100)
	488	0.1	5	17	5	1 (20)	0 (0)
	488	0.1	10	17	5	5 (100)	0 (0)

Table 2. Full-term development of transferred embryos following super-resolution imaging

mRNA injected	Optical wavelength (nm)	Optical intensity (mW)	Time intervals (min)	Imaging period (h)	No. of embryos examined	No. (%) of 2-cell embryos	No. of recipients	No. (%) of pups
Histone H2B-mCherry	-	-	-	17	22	22 (100)	5	8 (36.4)
	561	0.1	5	17	8	7 (87.5)	2	1 (14.3)
	561	0.1	10	17	15	15 (100)	3	7 (46.7)